PREDICTION OF TEMPERATURE FIELD DISTRIBUTION IN A GAS TURBINE USING A HIGHER ORDER NEURAL NETWORK

Jan Pařez*, Patrik Kovář, Adam Tater

Czech Technical University in Prague, Faculty of Mechanical Engineering, Center of Aviation and Space Research, Technická 4, Prague 6, Czech Republic

* corresponding author: `jan.parez@fs.cvut.cz`

Abstract. This paper presents the prediction of temperature field distribution in a single annular section using an artificial neural network (ANN). This temperature distribution is non-uniform on the outer tube due to continuous natural convection and radiation caused by the homogeneous steady-state heating of the inner tube, which represents the hot gas flow path through the turbine. The outer tube represents the case of a gas turbine. This temperature is important for the electronic components attached to the engine or the overall engine deformation. The presented approach allows for a quick estimation of the temperature distribution without the need to perform time consuming computational fluid dynamics (CFD) simulations. This can greatly accelerate the design and development of gas turbines. A machine learning approach is applied to an extensive set of CFD simulations under different operating conditions and geometry setups.

Keywords: Gas turbine cooling, heat transfer, artificial neural network, natural convection.

1. Introduction

The cooling process and temperature distribution of solid parts in gas turbines is critical to their reliable operation and maximum performance. High temperatures in the combustion chambers and hot section of the engine can adversely affect the lifespan of parts and accessories, trend/health monitoring, and electronic control system components. Therefore, it is important to design and implement cooling systems that ensure optimal temperature conditions and protect key components attached to the engine case. These components have maximum temperature limits, and exceeding these limits can cause damage and affect engine operation.

Nakayama [1] introduced the issue of maximum temperature for electronic devices attached to gas turbines. A significant problem is the temperature sensitivity of the gas turbine rotor, which affects the dynamic behaviour of the engine, or in the worst case, rotor thermal lock. Uneven cooling can cause shaft deflection known as rotor thermal bow. Many papers have addressed the problem of rotor thermal deformation. Chatterton [2] presented the results of a diagnostic method of multiple linear regression models for temperature field prediction and analysis that can be very useful for maintenance prediction.

Uneven temperature distribution during post shutdown cooling on the engine casing has been studied by Yu et al. [3], resulting in deformation of the rotor system. Different geometry and environmental settings on the temperature field distribution were experimentally verified. The temperatures cause structural deformation and cause mass non-uniformities, resulting in vibrations. Peng [4] presented extensive experimental measurements with heat distribution on

the rotor during cooling and thermal deflection prediction. A computationally intensive simulation was performed by Padilla [5] using the large eddy simulation (LES) for the transient and turbulent flow region. Improvement of the numerical prediction of RANS using the natural convection heat transfer method in gas turbines was also presented by Pilkington [6] who also performed measurements on a large gas turbine test rig. In his work, he compared several models and proposed a modification of the GGDH model, which he called GGDH+, that takes into account the buoyancy effects on the turbulent heat flux and is comparable to the LES results.

There are several heat management methods of cooling gas turbines. These include internal cooling, where a coolant (typically air or liquid) is directly supplied to cavities within the turbine's internal structure [7], and external cooling, which utilises the flow of coolant around the surface of turbine components [8].

Another technique is film cooling, where a thin layer of coolant is applied to the surface of the components to reduce their temperature [9]. These methods are combined and optimised to achieve the best cooling effect and minimise thermal stress on turbine components. In addition, there are areas within the engine where spontaneous natural convection occurs. This has a significant effect on the temperature distribution on the engine case.

Earlier research by Pařez et al. [10–12] was also focused on a numerical study of the effect of heat transfer in a double annulus. Methods to improve the uniformity of the temperature field were proposed and the numerical model was experimentally verified on several geometries at different temperature settings. Proper temperature distribution and effective cooling

are crucial for achieving long life and reliability of gas turbines. Therefore, a considerable attention is given to the design and optimisation of cooling systems to minimise the risk of overheating and ensure optimum operating temperatures. This increases the performance and lifespan of turbines and ensures reliability in various industrial applications.

However, the problem of predicting non-uniform temperature fields arises from their computational complexity. Therefore, it is necessary to find an efficient tool for fast and accurate prediction of temperature distribution in different engine modes, which is the scope of this paper. An extensive set of CFD simulations under different operating conditions and geometrical setups was performed in order to obtain a training data set for the machine learning approach. A higher order neural network (HONN) was chosen as the approximator for the task. Its advantage is that it has fewer degrees of freedom and therefore fewer parameters to optimise during the learning process. Other advantages include faster convergence and more accurate results due to its non-linear nature as it was presented in [13–15].

2. TASK

The case presented is considered to be the temperature field distribution at steady-state engine operation. The temperature field distribution depends only on the temperature in the current flow path due to operating conditions. A uniform temperature distribution in the flow path is considered, thus giving a boundary condition of constant temperature at the inner edge of the inner tube. The geometry of this case is then simplified to a single annulus between the inner and outer tube as it can be seen in Figure 1. Due to the constant temperature at the edge of the inner tube, a steady-state temperature distribution is sought on the outer tube.
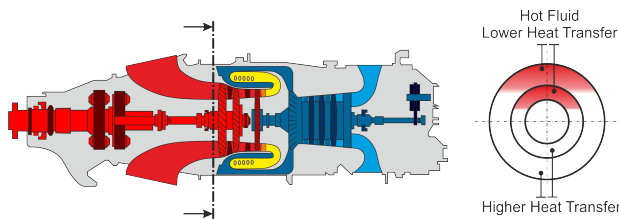

FIGURE 1. Natural convection in aircraft engine.

2.1. GEOMETRY

The computational geometry is based on a 2D cross-section of a turboprop engine. It consists of an inner tube representing the flow path boundary of the running engine, labelled Tube 1 in Figure 2, and an outer engine case, labelled Tube 2 in Figure 2. The outer diameter D_2 is constant for all the calculated cases. The inner diameter D_1 is varied according to the values in Table 1. The thickness of the outer tube t_2 is

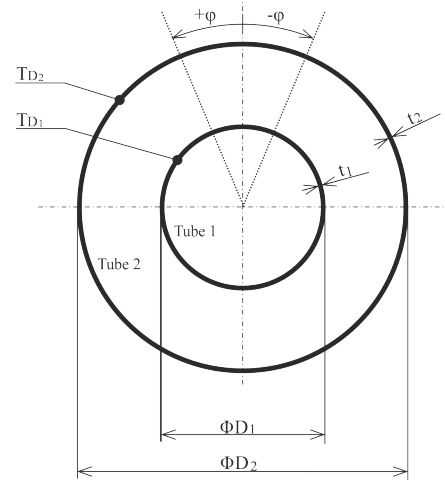chosen in the range given in Table 1. The thickness of the inner tube is assumed to be constant $t_1 = 1\,\text{mm}$.

FIGURE 2. Scheme of the physical domain with its parameters.

Dimension	Value	Unit
D_2	400	[mm]
t_2	$\{1, 2, 3\}$	[mm]
D_1/D_2	$\{0.5, 0.6, 0.7, 0.8, 0.9\}$	[1]
T_{D_1}	$\{773.15, 873.15, 973.15\}$	[K]

TABLE 1. Operating parameters.

2.2. OPERATIONAL CONDITIONS

The operating conditions and engine modes define the temperature field for the worst case, namely the turbine section. The temperatures are based on steady-state operating conditions in the three engine modes generalised and rounded to the nearest hundred Celsius degrees. The first mode is the idle mode, the next is the cruise mode and the last is the maximum take-off mode. The steady-state uniform temperature values for the flow path are marked as T_{D_1} in Table 1 and remain constant throughout the calculation.

The temperature response of the temperature distribution on the outer case of the engine is marked as T_{D_2}. Referring to previous considerations, the desired function represented by neural network $\mathcal{N}(\bullet)$ is assumed in the form

$$\mathcal{N}(\bullet) \approx T_{D_2} = f(D_1/D_2, t_2, T_{D_1}, \varphi). \qquad (1)$$

2.3. COMPUTATIONAL METHODS AND DOMAIN DESCRIPTION

In this section, we focus on computational techniques, the specific domain under consideration, meshing, and the associated spatial discretisation error. All calculations were carried out using the Ansys® Fluent software, using fully structured meshes generated through the blockMesh utility available in the OpenFOAM®

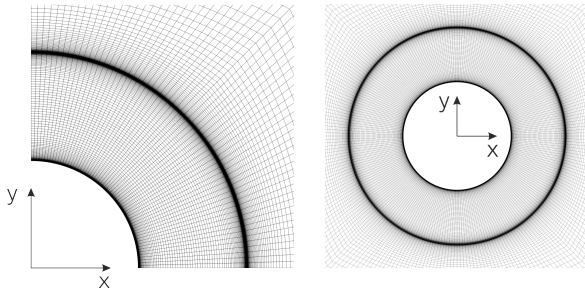package. The computational mesh is shown in Figure 3.

Figure 3. Computational mesh with detail on the refinement near walls.

In order to effectively model turbulent flow in practical engineering scenarios, the Navier-Stokes equations necessitate the implementation of Reynolds and Favres averaging. This procedure results in the formulation of the unsteady Reynolds-averaged Navier-Stokes (URANS) equations, as elucidated by Wilcox [16]. These URANS equations encompass the Reynolds stress tensor, necessitating a supplementary closure. Consequently, we adopt the two-equation Generalised $K - \omega$ (GEKO) turbulence model [17]. These equations can be written as

$$\frac{\partial \rho}{\partial t} + \nabla \cdot (\rho \vec{u}) = 0,$$

$$\frac{\partial(\rho \vec{u})}{\partial t} + \nabla \cdot (\rho \vec{u} \otimes \vec{u}) + \nabla p - \nabla \cdot \vec{\vec{\tau}} = \rho \vec{g}, \qquad (2)$$

$$\frac{\partial(\rho E)}{\partial t} + \nabla \cdot ((\rho E + p)\vec{u} - \vec{\vec{\tau}} \cdot \vec{u}) = -\nabla \cdot \vec{q},$$

where the heat flux $\vec{q}$ is composed of the conduction part $\vec{q}_c$ and the radiation part $\vec{q}_r$. To address the radiation part, we introduce an extra radiative transfer equation into the simulation. Given that the system pertains to surfaces that are gray and diffuse, the heat exchange between these surfaces depends on factors such as their dimensions, separation distance, and orientation. Moreover, we consider processes like absorption, emission, and scattering of radiation. In this context, we implement the discrete ordinates (DO) radiation model [18].

This results in a system of seven partial differential equations. Four of these equations come from system (2), another two equations modelling the transport of turbulent kinetic energy and the specific dissipation of turbulent kinetic energy come from the turbulence model and the last equation models the radiation.

To finally close the governing equations modelling the natural convection as discussed earlier, we can use a selection of equations of state. One such approach is the Boussinesq approximation [19], which postulates that density is contingent upon temperature in the following manner

$$\rho \approx \rho_0 + \frac{\partial \rho}{\partial T}\bigg|_{T_0} (T - T_0). \qquad (3)$$

In certain cases, this method loses its validity, particularly when dealing with substantial temperature differentials where linearisation becomes inadequate. In such instances, a more precise approach is employed to ascertain the relationship between the density and the temperature. An appropriate closure formula for describing natural convection with significant temperature gradients, as outlined in the work by Mayeli [20], involves the utilisation of the weakly compressible gas equation of state, which is defined as follows

$$\rho = \frac{p_{ref}}{RT}, \qquad (4)$$

where $p_{ref} = 101\,325\,\text{Pa}$ is the reference pressure, which stays constant throughout the simulation. Therefore, density ρ is only a function of temperature. This equation of state was used in all simulations.

For the solution of the equations governing natural convection including turbulence and radiation as described earlier, we opted for the finite volume method. Within this Ansys® Fluent framework, we have chosen the pressure-based approach using the Rhi-Chow numerical flux [21], over the density-based approach which uses numerical fluxes from AUSM [22], HLL [23] or rotated-hybrid [24] Riemann solver families. Next, a "coupled". scheme was applied to handle the pressure-velocity coupling. Gradients were calculated using the cell-based least squares approach. Throughout the simulations, all spatial discretisation schemes were configured to achieve second-order accuracy. Furthermore, we employed a second-order implicit pseudo transient time formulation. All simulations were performed until steady states were reached.

The schematically pictured computational task can be seen in Figure 4. This representation is misleading in terms of dimensions. In reality, the side of the square is approximately 12 times greater than the large diameter of the outer tube. Tubes' thicknesses are also enlarged in Figure 4.
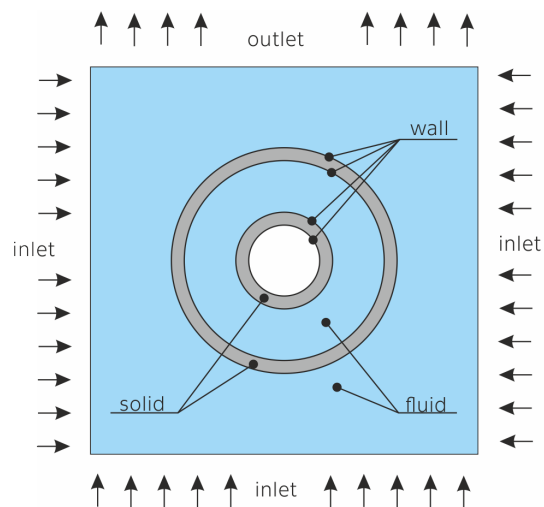

Figure 4. Schematic computational domains with marked boundary conditions.

The whole computational task is composed of four subdomains. Two of them, coloured blue, model air as a fluid. The other two, coloured in grey, model steel tubes as a solid. These subdomains are connected with coupled walls and the heat conduction through the tubes is fully modelled. The square-shaped subdomain represents the atmosphere with inlet and outlet boundary conditions. The variables prescribed at the inlet were the total pressure, temperature, and angle of the velocity vector, $101\,325\,\mathrm{Pa}$, $293.15\,\mathrm{K}$, and perpendicular to the boundary, respectively. The variable prescribed at the outlet was the static pressure with a value of $101\,325\,\mathrm{Pa}$. Constant temperature T_{D_1} was prescribed at the inner edge of the inner tube. Zero velocity magnitude was also specified on all walls.

The distribution of the temperature and velocity magnitude field calculated using CFD in the single annulus due to natural convection and radiation is shown in Figure 5 and Figure 6.
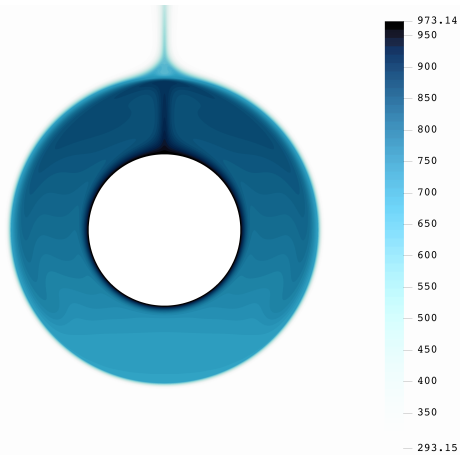

Figure 5. Temperature field distribution for case $D_1/D_2 = 0.5, t_2 = 1\,\mathrm{mm}, T_{D_1} = 973.15\,\mathrm{K}$.

Figure 6. Velocity magnitude field distribution for case $D_1/D_2 = 0.5, t_2 = 1\,\mathrm{mm}, T_{D_1} = 973.15\,\mathrm{K}$.

2.3.1. Grid convergence study

Analysing mesh convergence in a simulation is a straightforward approach to gauge the level of discretisation error within a numerical simulation. This method entails conducting the simulation on progressively finer meshes. As the mesh becomes more refined, spatial discretisation errors should gradually diminish, asymptotically approaching zero, except for negligible computer rounding errors.

For the scope of this study, it is necessary to designate a specific scalar quantity. In this instance, we have selected the volume average of temperature on the outer tube, denoted as $\mathcal{T}$, to serve this purpose. We generated three progressively finer meshes, maintaining a refinement ratio of $r = 2$. This means that the finer mesh contains twice as many cells as the coarser mesh in both spatial directions. Table 2 provides a comprehensive listing of all three meshes, along with their respective cell counts.

Mesh label	"1"	"2"	"3"
Normalised mesh spacing	4	2	1
Number of cells	53 504	214 016	856 064

Table 2. Parameters of meshes generated and used in convergence study.

Given that the parameter r remains constant, we can determine the order of convergence $\mathcal{O}$ shown in Equation (5) using Roache's method, as described in [25], by directly utilising three solutions in the following manner

$$\mathcal{O} = \frac{\ln\left(\frac{\mathcal{T}_1 - \mathcal{T}_2}{\mathcal{T}_2 - \mathcal{T}_3}\right)}{\ln(r)}. \tag{5}$$

Once the convergence order has been assessed, we can proceed to apply Richardson extrapolation, as elucidated by Zlatev et al. [26], to the two most refined meshes. This method leverages these meshes to derive an estimate for the "exact" solution at zero mesh spacing, represented as Equation (6)

$$\mathcal{T}_{ext} = \mathcal{T}_3 + \frac{\mathcal{T}_3 - \mathcal{T}_2}{r^{\mathcal{O}} - 1}. \tag{6}$$

As per Roache's guidance mentioned in [25], the Grid Convergence Index (GCI) stands out as a favoured means of approximating discretisation errors. It quantifies the percentage by which the computed value deviates from the asymptotic numerical value, essentially delineating an error margin for the solution's proximity to the asymptotic value. Additionally, it provides insight into how the solution might alter with further grid refinement. A diminutive GCI value suggests that the computation resides within the asymptotic range. The computation of GCI can be performed using Equation (7)

$$\mathrm{GCI} = \frac{\mathrm{F_S}|\epsilon|}{r^{\mathcal{O}} - 1} \cdot 100, \quad \epsilon = \frac{\mathcal{T}_{\mathrm{finer}} - \mathcal{T}_{\mathrm{coarser}}}{\mathcal{T}_{\mathrm{finer}}}. \tag{7}$$

In accordance with Wilcox's recommendation [16], a safety factor denoted as F_S is advised to be set at $F_S = 1.25$ when employing three or more grids. From the utilisation of three meshes, we can derive two Grid Convergence Indexes, denoted as GCI_{12} and GCI_{23}. The results of the mesh convergence study are listed in Table 3. These results were obtained for the case $D_1/D_2 = 0.5$, $T_{D1} = 973.15\,K$ and $t_1 = 1\,mm$.

$\mathcal{T}_1$	$\mathcal{T}_2$	$\mathcal{T}_3$
687.569	685.805	685.274
$\mathcal{O}$	GCI_{12}	GCI_{23}
1.73	1.4 %	0.4 %

TABLE 3. Results of the mesh convergence study.

Based on these results, the mesh labeled as "1" was chosen for further computations as the discretisation error is sufficiently low. Thus, the error band is approximately $\pm 9.6\,K$ around the $\mathcal{T}_1$ value.

2.4. TEMPERATURE FIELDS

In order to obtain the training data set for neural network and replace experimental measurement, various numerical simulations with different geometrical setups and boundary conditions on the inner tube were performed as listed in Table 1.

Trends of the temperature field distributions around the outer tube were observed on both inner and outer surfaces. The setup with ratio $D_1/D_2 = 0.8$, $t_2 = 1\,mm$ and $T_{D1} = 873.15\,K$ is shown in Figure 7. Temperature distribution is a function of the angle φ where 0 indicates the highest point of the investigated geometry (see Figure 2).
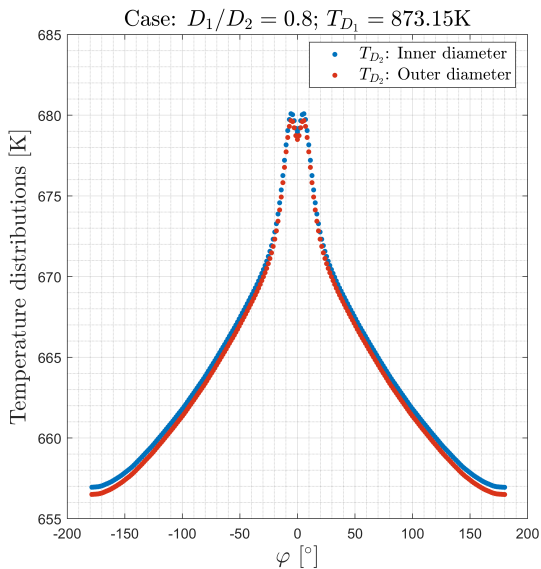

FIGURE 7. Results of the CFD: temperature field distribution observed at the surfaces of the inner tube.

To simplify the task, some assumptions were accepted. Firstly, the temperature is assumed to be symmetrical along the vertical axis, thus the data with corresponding angular coordinate are averaged. And secondly, due to small temperature differences on the inner and outer edge of the outer tube and due to error band arising from the CFD discretisation error (see Table 3), it is assumed that the influence of the inner tube thickness can be neglected, so that temperatures on these edges are also averaged.

Part of the training data set, representing one batch of D_1/D_2 ratios and boundary conditions T_{D_1} prescribed on the inner tube permutations with constant thickness t_2, is shown in Figure 8. The directions of individual parameter value growth are indicated by arrows, while the resulting part of the training data set is visualised against the number of the sample. Each cluster of data represents a single CFD simulation. As one can see, the behaviour is non-linear, which is a suitable task for the neural network learning.
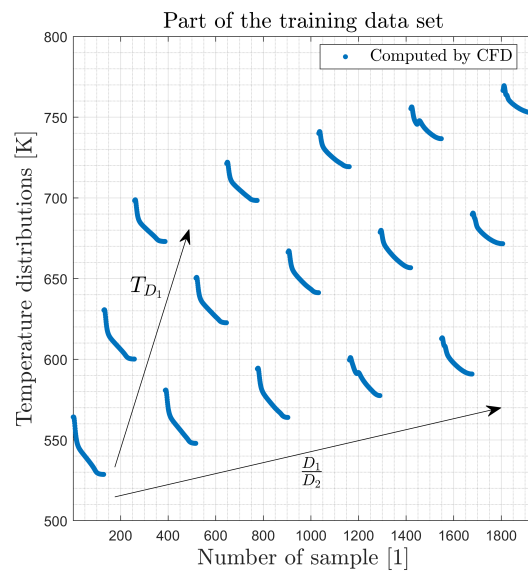

FIGURE 8. Part of the training data set with accepted simplifications.

2.5. CFD EXPERIMENTAL VALIDATION

The accuracy of the proposed numerical CFD model was verified and validated experimentally using an experimental setup. The time dependence of the temperature fields was observed and compared with the computational model. The results of this experiment and validation were presented by authors in [10, 12].

The same CFD model was used in the current calculation. A good agreement between the experiment and the numerical model was achieved with an error of the order of a few percent.

3. NEURAL NETWORK APPROACH

From a mathematical point of view, processing the information within neuron consists of two separate mathematical operations [27]. The first, synaptic operation, contains weights of the synapse, which

represents storage of knowledge and thus the memory from previous knowledge.

The second is somatic operation, which provides various mathematical operations, such as thresholding, non-linear activation, aggregation, etc. The neural output of the unit $\widetilde{y}$ is then scalar as it is indicated in Figure 9 and expressed by following Equation (8)

$$\widetilde{y} = \sigma(s). \tag{8}$$

Let us assume N-th order neural unit, then the product of a synaptic operation can be written as Equation (9).

$$s = w_0 x_0 + \sum_{i=1}^{n} w_i x_i + \sum_{i=1}^{n}\sum_{j=i}^{n} w_{ij} x_i x_j + \ldots$$
$$+ \sum_{i_1=1}^{n} \cdots \sum_{i_N=i_{N-1}}^{n} w_{i_1 i_2 \ldots i_n} x_{i_1} x_{i_2} \ldots x_{i_n}, \tag{9}$$

where $x_0 = 1$ denotes the threshold and n stands for the length of the input feature vector.
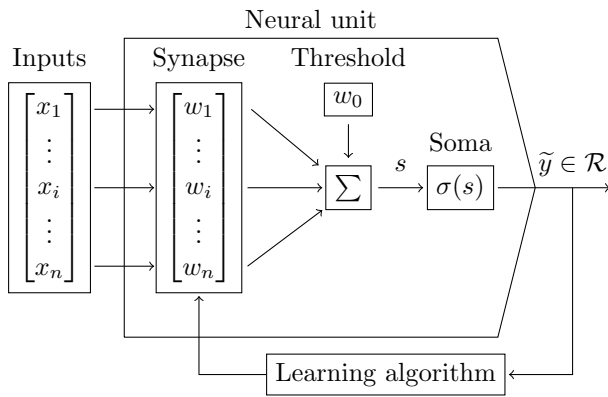

FIGURE 9. Neural network: single neural unit.

Since the desired outputs are predetermined, the process of machine learning is termed as supervised learning. This involves learning a function that connects input to output using a cost function $\vec{e}$.

As we can see, the neural output is strongly dependent on the neural memories represented by vector of the weights $\overrightarrow{W}$. So, to help the neural unit learn, the information processing needs to be structured appropriately. Batch Levenberg-Marquardt algorithm for updating weights [27] is utilised in present work

$$\overrightarrow{W} = \overrightarrow{W} + \Delta\overrightarrow{W}, \tag{10}$$

where

$$\Delta\overrightarrow{W}^T = -\left(\overrightarrow{\overrightarrow{J}}^T \overrightarrow{\overrightarrow{J}} + \frac{1}{\mu}\overrightarrow{\overrightarrow{I}}\right)^{-1} \overrightarrow{\overrightarrow{J}}^T \vec{e}. \tag{11}$$

Coefficient μ is the learning rate, $\overrightarrow{\overrightarrow{I}}$ is $n_w \times n_w$ identity matrix, n_w the number of weights and $\overrightarrow{\overrightarrow{J}}$ represents $n \times n_w$ Jacobian matrix.

Usually, the training data set is divided into three subsets. The first, training set, which serves for learning and updating weights. The second is the validating set. After each epoch of the learning algorithm, error estimation is performed on this subset in order to avoid neural unit overfitting. The training continues until the validating error increases. The third part is called the testing set, which measures the error after learning is terminated.

According to previous considerations, the desired function is assumed in a form of Equation (1). The neural network was assembled by five neurons with third order synaptic operation and bipolar sigmoid activation in the first layer and single second order neuron with linear activation in the output layer as it can be seen in Figure 10. Error propagation through the network is performed by Gupta et al. [28] using multilayer backpropagation algorithm.
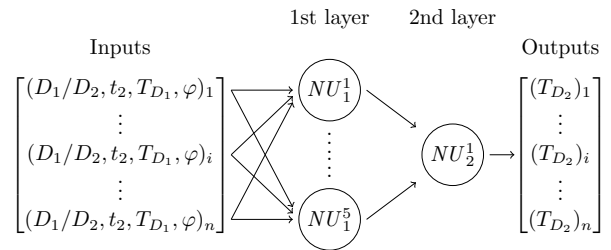

FIGURE 10. Neural network: shallow neural network.

4. RESULTS

All samples in the obtained data set (5 805 in total) were normalised using the *minmax* method within a range of $\langle 0; 1\rangle$ Learning rate was set to a constant value $\mu = 0.2$ and the total number of epochs was set to 1 000. In Figure 11, it can be seen that the validation error reached its minimum at 48-th epoch with a test error of 2.1338e-5 in the norm space.
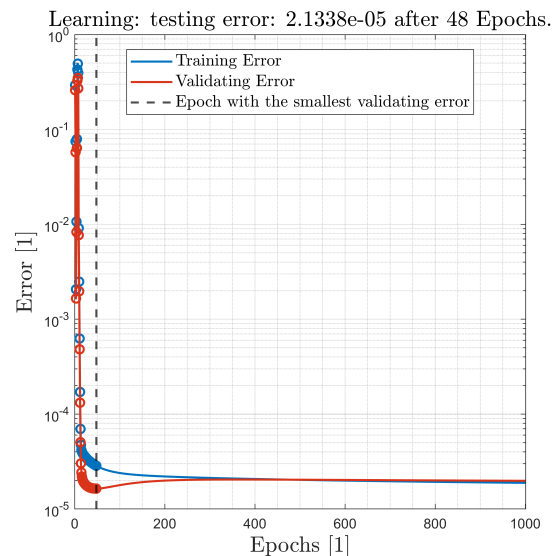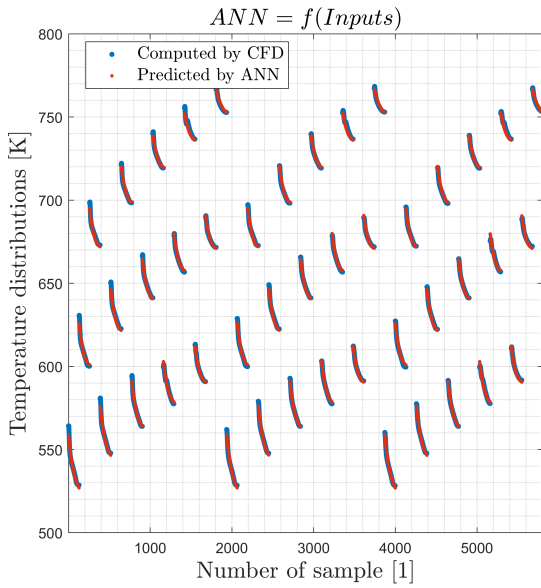

FIGURE 11. Results: progress of the learning.

FIGURE 12. Results: comparison of neural outputs against training data set in the sample space.
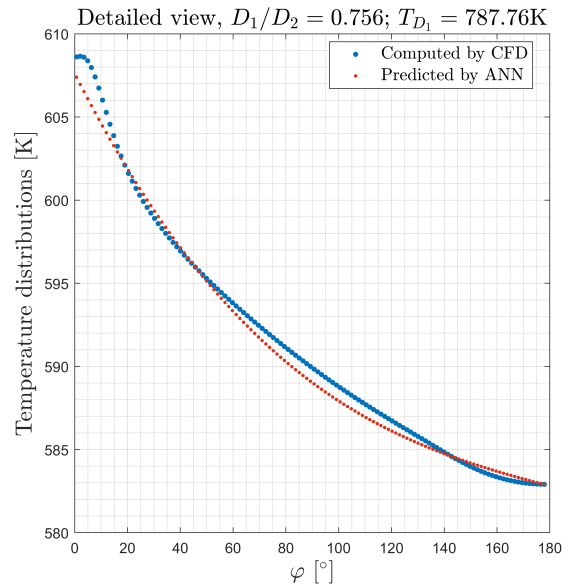

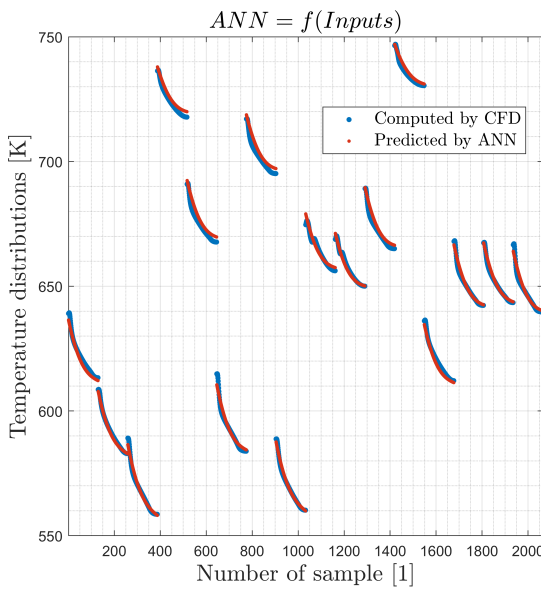FIGURE 14. Results: comparison of neural outputs against testing data set - the best match.

FIGURE 13. Results: comparison of neural outputs against testing data set obtained using LHS.
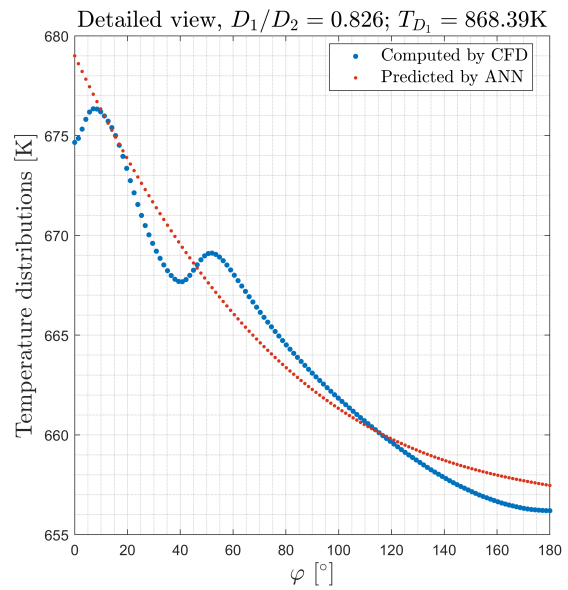

FIGURE 15. Results: detailed comparison of neural outputs against testing data set - the worst match.

Weights set in this learning epoch were evaluated as the best approximation of the task before any possible overfitting. There is a graphical comparison of the neural output against the training data set shown in Figure 12. It can be seen that the neural outputs are in good agreement with the training data set. The mean squared error (MSE) reached 1.548 in the sample space, *i.e.* not norm space.

Latin hypercube sampling (LHS) was used to generate the data set. The strategy chosen was 16 samples with a maximum sum of distances in the sample space [29]. A comparison of the neural outputs against the testing data obtained using LHS is shown in Figure 13.

The MSE for the testing data was 2.41.

In Figure 14, there is a graphical comparison of the obtained prediction using neural network. It can be seen that the trend of the temperature field copies the trend of the temperature distribution obtained using a standard CFD approach. The maximum difference between the prediction and the true distribution is $2.1\,\mathrm{K}$, which is in a sufficient error band, according to [30] and performed convergence grid study.

The worst case in terms of matching the testing data set is shown in Figure 15. It is the case when the ratio $D_1/D_2 = 0.826$ and the temperature at the inner tube was set to $T_{D_2} = 868.39\,\mathrm{K}$.

The maximum difference can be observed at the top of the inner tube, *i.e.* at $\varphi = 0°$, where the difference between the prediction and the data obtained through CFD reached $4.3\,\text{K}$, which is up to the measurement error limits described in [30] but still within the error band established by GCI.

The oscilation in the area $\varphi = \langle 30; 60 \rangle°$ is not correctly captured bu the prediction differs from the CFD data by less than $2.0\,\text{K}$ which is also within the sufficient error band.

5. CONCLUSION

In order to eliminate time-consuming CFD simulations and accelerate the design of aircraft engines, this paper presents an approach to modelling the temperature field distribution on the outer tube in a single annulus, representing an aircraft engine section, using a higher order neural network. Based on a gas turbine section, various geometrical setups were prepared for the CFD simulations to obtain a training data set. Moreover, three engine steady-state modes, standing for idle, cruise and maximal take-off, were considered. A grid convergence study was performed on a chosen case in order to detect error band arising from the CFD. A large data set was obtained after comprehensive set of CFD simulations. Some simplifications, based on the results of the convergence study, were accepted as described in Section 2.4.

A higher order artificial neural network architecture was also described. The learning was successful with a training error, measured by MSE, of 1.548 in the sample space, which is a sufficiently low error given the error band given by the CFD simulations. The results of the learning were also tested on the testing data set, which consisted of sixteen cases generated using Latin hypercube sampling. The MSE performed on the testing data set reached 2.41, which is also within the error band and is also covered by the measurement uncertainty of the thermocouple as described in [30].

Further work should aim at more complex geometry, more accurate CFD simulations and transient flow cases. The next step is to use finite element methods for deformation analysis and to develop a coupled solver that will allow faster analysis, and thus faster design of the device.

LIST OF SYMBOLS

φ Angle [°]
D_1 Inner tube diameter [mm]
T_{D_1} Inner tube temperature [K]
t_1 Inner tube thickness [mm]
D_2 Outer tube diameter [mm]
T_{D_2} Outer tube temperature [K]
t_2 Outer tube thickness [mm]
t Time [s]
$\mathcal{T}$ Volume average of temperature [K]
ρ Density [kg m^{-3}]
$\mathcal{O}$ Order of convergence [1]

p Static pressure [kg m^{-1}s^{-2}]
p_{ref} Reference static pressure [kg m^{-1}s^{-2}]
E Specific total energy [m^2 s^{-2}]
R Specific gas constant [m^2 s^{-2}]
r Refinement ratio [1]
$\vec{u}$ Velocity [m s^{-1}]
$\vec{q}$ Heat flux [m s^{-1}]
$\vec{q}_r$ Radiation heat flux [m s^{-1}]
$\vec{q}_c$ Conduction heat flux [m s^{-1}]
$\vec{g}$ Gravitational acceleration [m s^{-2}]
$\vec{e}$ Cost function [1]
$\overset{\Rightarrow}{\vec{I}}$ Identity matrix [1]
$\overset{\Rightarrow}{\vec{J}}$ Jacobian matrix [1]
n Length of input feature vector [1]
n_w Number of weights [1]
x_0 Neural threshold [1]
$\widetilde{y}$ Neural output [1]
$\vec{W}$ Vector of the weights [1]
$\sigma(\cdot)$ Activation function [1]
μ Learning rate [1]

REFERENCES

[1] W. Nakayama. Thermal management of electronic equipment: A review of technology and research topics. *Applied Mechanics Reviews* **39**(12):1847–1868, 1986. https://doi.org/10.1115/1.3149515

[2] S. Chatterton, P. Pennacchi, A. Vania. An unconventional method for the diagnosis and study of generator rotor thermal bows. *Journal of Engineering for Gas Turbines and Power* **144**(1):011024, 2022. https://doi.org/10.1115/1.4052079

[3] X. Yu, Z. Liu, Z. Zhou, et al. Experimental research on the characteristics of thermal bow in an aeroengine HP spool. In *Proceedings of the ASME Turbo Expo 2020: Turbomachinery Technical Conference and Exposition*, vol. 1: Aircraft Engine; Fans and Blowers. ASME, 2020. https://doi.org/10.1115/GT2020-14109

[4] H. Peng, Z. Zhou, J. Feng, et al. Prediction of the thermal bow of rotor based on the measured displacement and temperature. *International Journal of Distributed Sensor Networks* **16**(10), 2020. https://doi.org/10.1177/1550147720962993

[5] E. Padilla, A. Silveira-Neto. Large-eddy simulation of transition to turbulence in natural convection in a horizontal annular cavity. *International Journal of Heat and Mass Transfer* **51**(13-14):3656–3668, 2008. https://doi.org/10.1016/j.ijheatmasstransfer. 2007.07.025

[6] A. Pilkington, B. Rosic, K. Tanimoto, S. Horie. Prediction of natural convection heat transfer in gas turbines. *International Journal of Heat and Mass Transfer* **141**:233–244, 2019. `https://doi.org/10.1016/j.ijheatmasstransfer.2019.06.074`

[7] B. Vijayaragavan, S. P. Asok, C. R. Shakthi Ganesh. Heat transfer characteristics of double pipe heat exchanger having externally enhanced inner pipe. *Acta Polytechnica* **63**(1):65–74, 2023. `https://doi.org/10.14311/AP.2023.63.0065`

[8] M. Gaffuri, P. Ott, S. Naik, M. Henze. Experimental investigation of sequential narrow impingement channels for turbine cooling. In *14th European Conference on Turbomachinery Fluid dynamics & Thermodynamics*. European Turbomachinery Society, 2021. `https://doi.org/10.29008/ETC2021-523`

[9] K.-I. Takeishi, S. Aoki. Contribution of heat transfer to turbine blades and vanes for high temperature industrial gas turbines part 1: Film cooling. *Annals of the New York Academy of Sciences* **934**(1):305–312, 2001. `https://doi.org/10.1111/j.1749-6632.2001.tb05864.x`

[10] J. Pařez, A. Tater, P. Kovář, et al. Influence of geometrical design on the cooling process of double annular turbine section. *International Journal of Engine Research* **24**(8):3707–3719, 2023. `https://doi.org/10.1177/14680874231167206`

[11] J. Pařez, P. Rohan, T. Vampola. Heat transfer in double annular due to natural convection. In *IOP Conference Series: Materials Science and Engineering*, vol. 1190, p. 012002. IOP Publishing, 2021. `https://doi.org/10.1088/1757-899X/1190/1/012002`

[12] J. Pařez, A. Tater, J. Polanskỳ, T. Vampola. Experimental and numerical study of natural convection in 3D double horizontal annulus. In *European Physical Journal Web of Conferences*, vol. 264. 2022. 01027. `https://doi.org/10.1051/epjconf/202226401027`

[13] P. Kovář, J. Fürst. Comparison of multilayer perceptron and higher order neural network's ability to solve initial value problem. In *24th International Scientific Conference Applied Mechanics 2023 Book of Abstracts*, pp. 55–58. Strojnícka fakulta STU v Bratislave, Bratislava, SK, 2023. ISBN 978-80-227-5294-7.

[14] P. Kovář, J. Fürst. Scalable activation function employment in higher order neural networks in tasks of supervised learning. In *Book of Abstracts 18th Youth Symposium on Experimental Solid Mechanics*, p. 37. Institute of Theoretical and Applied Mechanics, AS CR, Prague, CZ, 2023. ISBN 978-80-86246-66-6.

[15] P. Kovář, A. Tater, J. Pařez, J. Fürst. About the appropriate neural network size for the engineering applications. In *Proceedings of Computational Mechanics 2023*, pp. 91–94. University of West Bohemia, Pilsen, CZ, 2023. ISBN 978-80-261-1177-1.

[16] D. C. Wilcox, et al. *Turbulence modeling for CFD*, vol. 2. DCW industries La Canada, CA, 1998. `https://doi.org/10.1017/S0022112095211388`

[17] F. Menter, R. Lechner, A. Matyushenko. Best practice: generalized k-ω two-equation turbulence model in Ansys CFD (GEKO). *ANSYS Germany GmbH* 2019.

[18] S. Chandrasekhar. *Radiative transfer*. Dover Publications, 2013. ISBN 978-0-486-60590-6.

[19] J. Boussinesq. *Théorie analytique de la chaleur mise en harmonie avec la thermodynamique et avec la théorie mécanique de la lumière. Tome II : Refroidissement et échauffement par rayonnement; conductibilité des tiges, lames et masses cristallines, courants de convection, théorie mécanique de la lumière. 1903. xxxii, 625*, vol. 2. Gauthier-Villars, 1903.

[20] P. Mayeli, G. J. Sheard. Buoyancy-driven flows beyond the Boussinesq approximation: A brief review. *International Communications in Heat and Mass Transfer* **125**:105316, 2021. `https://doi.org/10.1016/j.icheatmasstransfer.2021.105316`

[21] C. M. Rhie, W.-L. Chow. Numerical study of the turbulent flow past an airfoil with trailing edge separation. *AIAA journal* **21**(11):1525–1532, 1983. `https://doi.org/10.2514/3.8284`

[22] M.-S. Liou, C. J. Steffen Jr. A new flux splitting scheme. *Journal of Computational physics* **107**(1):23–39, 1993. `https://doi.org/10.1006/jcph.1993.1122`

[23] A. Harten, P. D. Lax, B. van Leer. On upstream differencing and Godunov-type schemes for hyperbolic conservation laws. *SIAM Review* **25**(1):35–61, 1983. `https://doi.org/10.1137/1025002`

[24] J. Holman, J. Fürst. Rotated-hybrid Riemann solver for all-speed flows. *Journal of Computational and Applied Mathematics* **427**:115129, 2023. `https://doi.org/10.1016/j.cam.2023.115129`

[25] P. J. Roache. *Verification and validation in computational science and engineering*. Hermosa Albuquerque, NM, Albuquerque, NM, USA, 1998. ISBN: 978-0913478080.

[26] Z. Zlatev, I. Dimov, I. Faragó, Á. Havasi. Richardson extrapolation. In *Richardson Extrapolation*, vol. 2. De Gruyter, 2017. `https://doi.org/10.1515/9783110533002`

[27] M. Gupta, I. Bukovsky, N. Homma, et al. Fundamentals of higher order neural networks for modeling and simulation. In *Artificial Higher Order Neural Networks for Modeling and Simulation*, pp. 103–133. IGI Global, 2013. `https://doi.org/10.4018/978-1-4666-2175-6.ch006`

[28] M. Gupta, L. Jin, N. Homma. *Static and dynamic neural networks: from fundamentals to advanced theory*. John Wiley & Sons, 2004. ISBN 0-471-21948-7.

[29] M. Stein. Large sample properties of simulations using Latin hypercube sampling. *Technometrics* **29**(2):143–151, 1987. `https://doi.org/10.2307/1269769`

[30] Labfacility Ltd, Angmering, West Sussex, UK. *The New Labfacility Temperature Handbook*, v2.1 edn., 2006. TH0906.